This is the peer reviewed version of the following article: [Technical note: Mapping of trabecular bone anisotropy and volume fraction in 3D using µCT images of the human calcaneus. American Journal of Biological Anthropology 177, 3 p566-580 (2022)], which can be found at DOI: 10.1002/ajpa.24474

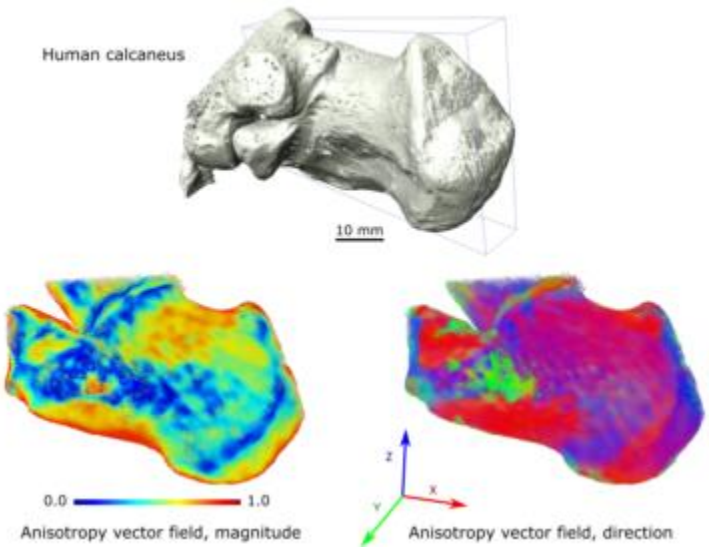

3D vector field-based mapping of trabecular anisotropy (human calcaneus)

141x96mm (72 x 72 DPI)

This is the peer reviewed version of the following article: [Technical note: Mapping of trabecular bone anisotropy and volume fraction in 3D using µCT images of the human calcaneus. American Journal of Biological Anthropology 177, 3 p566-580 (2022)], which can be found at DOI: 10.1002/ajpa.24474

Mapping of trabecular bone anisotropy and volume fraction in 3D using µCT images of the human calcaneus

Natalie Reznikov[1]*, Huilin Liang[2], Marc D. McKee[3,4], Nicolas Piché[5]

[1]Department of Bioengineering, Faculty of Engineering, McGill University, 3480 University Street, Montreal, Quebec, Canada H3A 0E9

[2]Faculty of Science, McGill University, 853 Sherbrooke Street West, Montreal, Quebec, Canada H3A 0G5

[3]Faculty of Dentistry, McGill University, 2001 Avenue McGill College, Montreal, Quebec, Canada H3A 1G1

[4]Department of Anatomy and Cell Biology, School of Biomedical Sciences, McGill University, 3640 University Street, Montreal, Quebec, Canada H3A 0C7

[5]Object Research Systems, 760 Saint Paul Street West, Montreal, Quebec, Canada H3C 1M4

Corresponding author: Natalie Reznikov natalie.reznikov@mcgill.ca

Running title: Mapping of trabecular anisotropy and volume fraction in 3D

Abstract

Objectives. Trabecular bone anisotropy, or preferential trabecular co-alignment, is a proxy for its long-term loading history. Trabecular anisotropy varies locally, thus rendering averaged calculations across an entire bone inutile. Here we present a 3D trabecular anisotropy mapping method using vector fields where each vector reflects the extent of local co-alignment of the elementary units of surface. 3D anisotropy maps of hundreds of thousands of vectors were visualized by their magnitude or direction. Similarly, volume fraction was mapped as 3D scalar fields.

Materials and Methods. We constructed anisotropy and volume fraction maps using micro-computed tomography of four presumably nonpathologic human calcanei and compared their anisotropy signature with the pathologically loaded calcanei in club foot and calcaneonavicular ankylosis.

Results. In the nonpathologic calcaneus, a pattern of four anisotropy trajectories was consistently identified as dorsal, plantar, Achilles', and peroneal bands. Both pathologic specimens deviated from the nonpathologic maps. The calcaneus in the congenital disused club foot showed very low local anisotropy values, no co-oriented bands and low volume fraction. The ankylosed calcaneus showed lower anisotropy than the nonpathologic calcaneus, but not to the same extent as the club foot, and patchy and high volume fraction. The directionality of co-oriented bands was barely discernable in the ankylosed calcaneus.

Conclusions. The anisotropy signature of the calcaneus, by magnitude and direction, is consistent with a kinetic loading pattern attributable to walking. The absence/loss of kinetic loading results in an absent/vanishing anisotropy signature. Such 3D mapping adds new dimensions to quantitative bioimaging and understanding of skeletal adaptation.

Keywords: Calcaneus, club foot, ankylosis, anisotropy, vector field, micro-computed tomography

Research highlights

- Trabecular bone anisotropy can be mapped in 3D using a vector field method
- 3D trabecular anisotropy mapped by direction and magnitude reveals covert anisotropy bands
- The anisotropy signature in the calcaneus reflects its loading trajectories

1. Introduction

Skeletal structures reflect the biomechanical history of an organism on both phylogenetic (evolutionary) and ontogenetic (individual) scales. Studying the outer morphology and inner architecture of bones has been an important empirical method in comparative anatomy, zoology, evolutionary biology, biological anthropology and pathology, providing a means to decipher the interplay of lifestyle, loading history, musculoskeletal crosstalk and health status. The quest to understand the trajectories of functional adaptation has been particularly fascinating and challenging in the context of locomotion. In this regard, the study of lower limb bone structure in bipedal humans is an important topic in many research fields. Our X-ray tomography work presented here applies to the human calcaneus a method of anatomically accurate and quantitative 3D visualization and mapping of *i*) trabecular anisotropy, and *ii*) bone volume fraction – plausibly the two most informative determinants of trabecular bone functional adaptation (Barak et al., 2013; Barak, Sherratt, & Lieberman, 2017; Goldstein, Goulet, & McCubbrey, 1993; Maquer, Musy, Wandel, Gross, & Zysset, 2015). The goal of this technical note is to introduce the principle of the 3D mapping method, and to illustrate its potential using two historical pathologic specimens of the human calcaneus, compared to four (presumably) nonpathologic ones. This is a proof of the method that can potentially be applied to biomechanical studies.

Anisotropy (Greek: "an" - non; "iso" - equal; "tropos" - way) – the opposite of isotropy – is a characteristic of having different properties in different directions, and/or of having preferred orientation of structural elements within a heterogeneous assembly. In the human skeleton, a 3D network of interconnected trabecular bone struts is consistently found, for example, in the interior of short bones or in the articulating portions of long bones (epiphyses and metaphyses). In different skeletal locations, the extent and degree of trabecular anisotropy varies. Along the lower limb, the degree of trabecular anisotropy increases in the proximo-distal direction (Saers, Cazorla-Bak, Shaw, Stock, & Ryan, 2016), thus reflecting the notion that a broad range of movement results in lower anisotropy, and a narrower range of movement results in higher anisotropy (Gibson & Ashby, 2001). Even in foetal/juvenile trabecular bone, anisotropic trajectories can be identified as evidence of phylogenetic adaptation (Skedros, Hunt, & Bloebaum, 2004). However, as a general trend within any particular skeletal element, the anisotropy of trabecular bone gradually increases from infancy to maturity (Acquaah, Robson Brown, Ahmed, Jeffery, & Abel, 2015; Ryan & Krovitz, 2006). The steady accrual of trabecular anisotropy reflects the magnitude, direction and continuity of the local forces acting upon it. Stereotypic loading of sufficient duration invariably generates a stereotypic pattern of trabecular anisotropy (Barak, Lieberman, & Hublin, 2011; Pontzer et al., 2006), and a natural example of this is the effect of bipedal locomotion on the calcaneus in children (Saers, Ryan, & Stock, 2020). The calcaneus is the largest of the seven tarsal bones of the foot. It articulates with the talus above, and the cuboid anteriorly, forming the shock-absorbing foot arch. Its distal portion – the tuberosity – is balanced between the Achilles tendon and the plantar fascia and normally bears roughly 40% of the load in bipedal locomotion (Rogers, 1988). The anisotropy signature of the foot bones develops in parallel with the reduction of kinematic instability in infants. The anisotropy signature is established by the time the gait pattern has stabilized: by age 9, anisotropy is high and uniform (Raichlen et al., 2015). Once the gait pattern is established, continuous and consistent loading maintains the pattern of trabecular anisotropy (Gefen & Seliktar, 2004). This corroborates the finding of converging anisotropy signatures in related species, if they experience comparable stimulation and similar loading patterns (Kuo, Desilva, Devlin, Mcdonald, & Morgan, 2013). However, in the development of the

anisotropy signature of any bone, phylogenetic and ontogenetic determinants are implicated, and we do not yet know with certainty the proportions of their contributions (Kivell, 2016).

Although the general rules of trabecular anisotropy can be formulated as *i*) increasing with age/time, *ii*) increasing with loading intensity, and *iii*) increasing with stereotypic function, there are nonetheless practical caveats in visualizing anisotropy. Besides the general factors affecting biomechanical responsiveness of bone, such as age or metabolic status, the accrual or loss of anisotropy is cumulative and slow, and it lags behind the onset of mechanical stimuli by years or decades. Concomitant loading trajectories result in distinct anisotropy bands (Sinclair et al., 2013; Wolff, 1892) that are best appreciated in 3D. Also, local anatomical features such as vascular canals or growth plate vestiges (the so-called epiphyseal scar) superimpose on the general anisotropy pattern. Therefore, insufficient consideration of a 3D anatomical shape, or even slightly inconsistent selection of sampling sites for anisotropy measurement, may affect accuracy and comparisons amongst samples (Doershuk et al., 2019; Maga, Kappelman, Ryan, & Ketcham, 2006), let alone the limited utility of single-number averaged metrics, such as an averaged degree of anisotropy over the whole specimen. Here, we demonstrate that local regional differences in trabecular bone anisotropy can be detected, mapped and quantified in 3D, and that these features can be correlated with the loading history of bone.

Previously, appreciation of the 3D spatial context has been the driving force for the design and development of integral, refined morphometric analyses of bone that operate on isosurface/mesh renderings of 3D images (Pahr & Zysset, 2009). A basic principle of holistic/integral mapping of morphometric parameters is that a "sampling probe" rasters a 3D image and records the anisotropy tensor, or the foreground/background ratio (the latter being equivalent to the trabecular bone volume fraction (Gross, Kivell, Skinner, Nguyen, & Pahr, 2014)). The resolution of the resultant 3D map, according to the homogenization theory, depends on both voxel size and feature size in an image. The diameter of the mapping probe being equivalent to 4-5 repetitions of features (*i.e*. average trabecular thickness plus average adjacent intertrabecular space ×5) results in rich and meaningful 3D visualization of, for example, volume fraction variation throughout homologous skeletal elements (Harrigan, Jasty, Mann, & Harris, 1988; Sukhdeo, Parsons, Niu, & Ryan, 2020). This approach resolves the uncertainty associated with discretization of the whole 3D image into subvolumes, and then calculating single-number descriptors for each subvolume (Reznikov et al., 2017). Although 3D mapping of the volume fraction within an entire anatomical entity is indeed informative allowing comparison of related species (Sukhdeo et al., 2020), the classic method of anisotropy measurement using the Mean Intercept Length (MIL) measurement (Odgaard, 1997, 2001) might be insufficiently sensitive if applied in the same 3D rastering manner. The MIL is a local statistical method in which the lengths of abstract lines passing through the foreground are averaged. Thus, it requires the sampling volume to exceed 4-5 intertrabecular spaces in diameter to yield consistent results. In this work, we present a new method based on local surface co-alignment, where the sampling volume of 1.5-2.5 mm in diameter is sufficient to generate a vector field of local anisotropy values. As a significant advancement for measuring in 3D space, the vectors in the resultant vector field can be visualized independently by magnitude or by direction. Additionally, as part of the same software plugin, we present quantitative 3D scalar mapping of volume fraction, which is conceptually similar to the method originally developed by Gross et al. (Gross et al., 2014; Sukhdeo et al., 2020). We illustrate the 3D mapping method for trabecular anisotropy and bone volume fraction using four presumably nonpathologic human calcanei, and two pathologic museum specimens of the calcaneus – the latter being

selected for their unique nature and the extraordinary extent of pathologic changes, as a proof of principle of the 3D mapping method.

Hypothesis. This study stemmed from our previous work (Reznikov et al., 2017) where we analyzed trabecular morphometric features of physiologically loaded human calcanei, and museum specimens of bound foot calcanei, which experienced loading in an altered orientation. In the bound-foot study, where the classic MIL anisotropy measurement was applied to 10 subvolumes of the calcaneus interior, we were expecting similar anisotropy values by magnitude, but different in orientation. Surprisingly to us, in pathologically loaded bound-foot calcanei, the anisotropy profile was inconsistent. Conversely, in the physiologically loaded, nonbound calcanei the anisotropy profile showed a recognizable S-shaped plot (Reznikov et al., 2017), even though plotting averaged MIL measurements over 10 segments is not comprehensive. That observation triggered the current hypothesis, whether it is the collective, consistent and repetitive stimulation by compressive forces (the body weight and ground reaction force) and tensile forces (pulling forces exerted by muscles and the plantar fascia) that collectively leave a morphological "track record" of the long-term function. We are testing this hypothesis by applying our custom-designed algorithm of 3D vector field-based anisotropy mapping to presumably physiologically loaded specimens from the earlier study, and two extreme cases of congenital and acquired disuse of the human calcaneus.

2. Materials and methods

2.1. Bone specimens

To illustrate the trabecular anisotropy and volume fraction mapping method for bone, we selected 6 skeletonized foot specimens that had been subjected to diverse loading scenarios *ante mortem*. The specimens included four putatively nonpathologic feet/calcanei from a university anatomy teaching collection, and two pathologic specimens of the human foot: a case of club foot (fixed talipes equino varus) and a case of calcaneonavicular ankylosis (Figure 1 A-C). Club foot is a complex developmental disorder that occurs in 1-6 cases per 1000 births, often as part of congenital syndromes, or as a family trait (Miedzybrodzka, 2003; Paton, Fox, Foster, & Fehily, 2010). The characteristic features of a club foot are adduction and supination in the varus position – resembling a twisted inwards, hand-like orientation. The degree of disability in club-foot patients varies from loss of mobility to fairly good compensation (Herd, Macnicol, & Abboud, 2004). Even after satisfactory correction, or poorly corrected or untreated cases, there is always a tendency for underloading of the hindfoot with a compensatory shift of the weight-bearing function to the lateral potion of the forefoot (Herd et al., 2004). Tarso-metatarsal and calcaneonavicular ankylosis (referred to as coalition, when congenital) is characterized by dorsiflection, longitudinal arch flattening and valgus deformity of the foot, as compensation for the limited mobility in the subtalar joint (Farid & Faber, 2019). Symptomatic patients adjust to pain and disability by limiting locomotion, or by developing antalgic gait (shortening the stance phase on the affected side). In comparison to nonpathologic human feet, the club foot and ankylosis cases (according to the Gordon Museum records) both presented severely limited mobility. Thus, we refer to them here as extreme cases of *congenital disuse* (club foot) or *acquired disuse* (ankylosis), in contrast with physiologic *use* as occurs in walking.

[Figure 1]

Both pathologic preparations were procured by the Gordon Museum of Pathology (King's College London, UK) in the second half of the XIXth century, and thus they predate the first applications of X-ray-based imaging (Figure 1 A and C). Such unique specimens of advanced deformities or chronic infections would be impossible to procure today – the availability of modern treatment methods simply does not allow extreme pathologies to develop to this extent. Although rare skeletal specimens from medical museums – originating from the pre-antibiotics/pre-public healthcare epoch – are an invaluable resource for structural studies, their nondestructive analysis using micro-computed tomography (μCT) is nontrivial. Many such historical museum specimens were mounted for morbid anatomy instruction at the macro-scale. Often, very crude and destructive mounting with metal fixtures was used, and the fragile interior of pathologic bones was easily damaged by this invasive destructive process. The presence of metal fixtures produces X-ray hardening and shadowing artifacts in 3D reconstructed images, and these often obscure fine osseous detail (Figure 1 B). The μCT scans of four nonpathologic calcanei were obtained as part of a previous study (Reznikov et al., 2017) using foot preparations from the Human Anatomy Unit of the Faculty of Medicine at Imperial College London (UK). These calcanei were assembled with other foot bones using metal wires, for gross anatomy teaching (Figure 1 D), that also resulted in X-ray beam-hardening artifacts (Figure 1 E). All μCT scans were acquired at the Imaging and Analysis Centre of the Natural History Museum in London (UK) using a Nikon Metrology HMX ST 225 scanner (Nikon, Tring, UK). The images were captured in 3142 projections using a 2000×2000 flat panel detector. The scanning parameters and conditions used were the following: tungsten anode, 0.25 to 0.5 mm copper filter, 700 to 1000 ms exposure time, tube peak voltage 180 kV, and current at 170 mA. The pixel size in the calcaneus tomograms varied between 0.033 and 0.047 mm, depending on specimen size. The focused calcaneus scans were used for analysis. In addition, the Gordon Museum preparations were scanned in full with a pixel size of 0.085 mm. The full-size scans were used for illustrative purposes. Reconstruction was performed using a Feldkamp back-projection algorithm with CTPro software (Nikon, Tring, UK).

2.2. Deep learning-based segmentation

Image processing was conducted using Dragonfly^{TM} v2020.1 software (Object Research Systems Inc., Montreal, Canada), under a noncommercial license (free-of-charge). All scans were segmented using a deep learning plugin with a broadly applicable UNet configuration of 5 layers (64 filters in the first layer and doubled in subsequent layers). The encoding UNet branch contained 10 convolutional filter layers (2 per layer, kernel size 3 × 3, stride 1, *same* padding) and 4 maximal pooling layers (kernel size 2 × 2, stride 2, and *valid* padding). The decoding branch contained alternating 4 concatenating layers, 8 convolutional layers and 4 upsampling layers. All convolutional layers were ReLU-activated. Abridged sets for UNet training were produced by marking roughly every 50th slice in the XY plane (using the software's *Mark slices* followed by *Derive image from marked slices* functions), attempting to include all the artifacts present in the raw images. Thus, the abridged training sets constituted about 2% of all data and were segmented manually using local thresholding and super-pixel-based edge detection. The segmentations were binary, with bone being labeled as the foreground and the rest being labeled as the background. A pair consisting of an abridged set (training input) and its binary segmentation (training output) comprised a training set for UNet training. All training sets were partitioned into 80% learning and 20% validation sets with moderate data augmentation (4-5 flip or rotate transformations, brightness enhancement). In

all cases, categorical cross-entropy loss function was utilized; the initial learning rate was set to 1, and consecutively decreased to 0.1, 0.01 and 0.001 automatically, when learning accuracy plateaued. In all cases, a patch size of 64 × 64 pixels was used with no overlap of adjacent patches – the stride-to-input was 1.0, the batch size was set to 64, and the number of epochs was set to 50 (but convergence was achieved around 20-30 epochs).

[Figure 2]

The club foot scan was the most affected by X-ray beam-hardening artifacts and thus required 3 cycles of output label refinement in order to achieve satisfactory accuracy, and the total number of training epochs was about 100. The ankylosis scan that did not contain metal fixtures but suffered from a very narrow dynamic range (appeared to be "dim") was segmented by a separately trained UNet model. All nonpathologic calcanei were segmented by the same UNet model that was retrained between the scans for about 20 epochs, with a minimal label refinement for each set. Figure 2 illustrates the surface rendering of two museum specimens in full. The magnified renderings of the calcaneus with a bounding box indicating the sagittal (or "would-be" sagittal in the case of club foot) orientation of the calcaneus.

2.3. 3D mapping of volume fraction (bone volume/ total volume, or BV/TV) and anisotropy

A bounding box (11 mm thick) was constructed in the sagittal plane through the middle of each reconstructed and segmented calcaneus. The height and width of the bounding box was adjusted to enclose only the calcaneus; the box was centered on the calcaneal tuberosity (Figure 2). In the Dragonfly software, the 3D mapping application operates in a designated window where the segmented image (region of interest, or ROI) and a fitted bounding box are imported. The application can be found in the main menu under *Utilities/Open Plugins/Bone Analysis*. Of note, the first steps of the mapping wizard include default steps for cortical-trabecular separation (Buie, Campbell, Klinck, MacNeil, & Boyd, 2007) and classic morphometric analysis (Bouxsein et al., 2010), that can be skipped by pushing the *Next* button. The mapping wizard menu contains 3 functions: *MIL* anisotropy vector field mapping, which is a 3D implementation of the classic MIL algorithm (Odgaard, 1997), *Surface Normals* anisotropy vector field mapping (original development for Dragonfly, by Object Research Systems), and *Volume Fraction* scalar mapping. All mapping functions operate on a binary image (ROI) and require a bounding box. The number of entries in the final 3D map (which is of the size of the bounding box) depends on the step size that corresponds to the rate of rastering the volume enclosed within the bounding box: the smaller the step size, the larger the number of measurements and the higher the density of the 3D map. At every step, a user-defined spherical portion of the 3D ROI is included in the calculation (sampling probe, as defined by its radius of influence). We used a step size of 0.5 mm and radius-of-influence of 1.5 mm for anisotropy, and a step size of 1.0 mm with a radius-of-influence of 1.5 mm for volume fraction. These values were selected following several rounds of algorithm optimization, when the parameters provided acceptable 3D map quality at the lowest computational cost. The step size of the anisotropy map was smaller than the step size of the volume fraction map (higher sampling density) for better visualization: vectors are plotted as miniature arrows. Having the arrows spaced too far away from each other in a 3D array makes the map less color-saturated (transparent), and the trajectories of co-oriented anisotropic bands are less conspicuous. Having enough arrows in a 3D vector maps renders them more "substantial" and easy to

view. Sparser sampling density can be used when computation resources are of concern, but the radius-of-influence should not be reduced below the modal size of a repeating feature (an average trabecula plus an average pore) times ×3. Anisotropy magnitude vector fields and volume fraction scalar field were color-coded using *Jet* LUT (look-up table), and anisotropy direction vector field was automatically color-coded as red-green-blue, corresponding to the cardinal axes X, Y and Z.

The surface anisotropy mapping method is based on automated construction of an interim surface mesh. The mesh is the interface between the foreground (region-of-interest or ROI) and the background, and it is triangulated. The mesh is populated by vectors perpendicular to the triangular surface units. The local surface anisotropy is calculated using a nominal sampling volume ("sphere of influence") that includes numerous triangulated surface units of mesh. The radius of the sampling volume is determined by the user, and for trabecular bone, the recommended radius value is between 1 and 2 mm, which is the approximate feature periodicity in human trabecular bone (*i.e*. frequency of repetition of trabeculae and pores). Below that value, an anisotropy map looks homogeneous and of high values because for a small "probe", the surface of a single trabecula is inevitably anisotropic (like for a human observer standing at ground level, the surface of the Earth appears flat and anisotropic, although the spherical shape of the Earth at a more distant scale of observation is obviously very isotropic). The collective magnitude of adjacent vectors is proportional to the local mesh surface face area (S) of the adjacent surface units that are co-aligned. Conversely, if the adjacent mesh units are oriented haphazardly, the unit vectors will likely cancel out. The algorithm uses a vector operation and projection of the face normals (n) on the principal axes (I) associated with the Eigenvectors of the inertia tensor of the sampling volume (Equation 1). For normalization of measurements, the coefficient of anisotropy (CA, ≥1) is converted into degree of anisotropy (DA, Equation 2).

$$CA = \frac{\Sigma_{i \in faces} s_i \cdot \left\| \vec{n}_i \times \vec{I}_0 \right\|}{\Sigma_{i \in faces} s_i \cdot \left| \vec{n}_i \cdot \vec{I_0} \right|} \qquad \textit{[Equation 1]}$$

$$DA = 1 - {}^{1}\!/_{CA} \qquad \textit{[Equation 2]}$$

A perfectly isotropic surface (such as that of a sphere) yields 0, and a perfectly anisotropic surface (as of an infinite line) yields a unity. Fractions of unity can also be expressed as a percentage. Both magnitude and directionality of the local surface anisotropy can be displayed as 3D vector fields using a color scale to represent the vector magnitude (for example, as a heat map: blue – 0, red – 1), or vector orientation with respect to the principal axes (for example, using an RGB color scheme: red - X, green - Y, blue - Z). As the spherical sampling volume rasters the requisite bounding box with a predefined step size, such anisotropy vector fields can be constructed over an entire volume of interest that is inscribed in the bounding box. The smaller the bounding box is, the faster the map construction is. Increasing the sampling radius lengthens the time of computation by the power of 3.

[Figure 3]

[Figure 4]

3. Results

Volume fraction and anisotropy analysis have long been the "gold standard" in skeletal biology studies. Considering that both these parameters vary quite broadly within any bone – thus reflecting trabecular tissue specialization in 3D – additional information can be revealed if volume fraction and anisotropy are plotted in 3D, at millimeter resolution. Figure 5 shows how 3D anisotropy signature and 3D volume fraction distribution relate to the shape of the calcaneus and its functional context.

[Figure 5]

Figure 6 compares the maps of three nonpathologic calcanei. Each map is constructed over a sagittal "slab" as defined by the bounding box (box not shown here) and contains about 300,000 measurements. Should the box enclose the full calcaneus, a larger map would be generated (at a higher computational cost).

[Figure 6]

Although the nonpathologic maps are not identical, a clear pattern emerges: in addition to the cortical shell contributing to the volume fraction values, subtalar trabecular bone clearly displays the highest volume fraction. The same subtalar area in anisotropy maps shows low anisotropy magnitude and inconsistent anisotropy direction. Overall, four major anisotropy trajectories can be consistently identified based on vector magnitude and direction: dorsal, plantar, the Achilles' bands in the sagittal plane, and the peroneal band in the transverse plane.

Figure 7 shows another (fourth) nonpathologic calcaneus in comparison with the club foot and ankylosed calcanei using the same layout of maps and color schemes. The fourth nonpathologic calcaneus appear consistent with the other three specimens in Figure 6. However, both pathologic specimens deviate from the appearance of the nonpathologic maps: the club-foot calcaneus shows uneven distribution of the volume fraction, which also has generally lower values. Generally lower local anisotropy values with a loss of consistent co-oriented bands are apparent in Figures 6 E and F. The ankylosed calcaneus shows generally higher volume fraction with patchy distribution, in comparison with the nonpathologic calcanei. The local anisotropy magnitude is generally lower than in the nonpathologic cases, but not to the same extent as in the club-foot calcaneus. In terms of directionality, the co-oriented bands are barely discernable in the ankylosed calcaneus.

[Figure 7]

Statistical analysis of volume fraction and anisotropy magnitude are given in Figure 8. Local anisotropy and volume fraction measurements were exported and plotted as histograms. The modal values of the volume fraction varied between 0.05 (club-foot calcaneus) and 0.175 (ankylosed calcaneus), with the four nonpathologic calcanei demonstrating intermediate values. The modal values of anisotropy between 0.6 and 0.675 characterized all four nonpathologic calcanei, whereas the ankylosed calcaneus has a lower modal value of 0.45, and the club-foot calcaneus has the lowest modal value of 0.31. We deemed it impractical to calculate standard deviation for the four nonpathologic specimens because n=1 in both pathologic categories (attributable to their rare, extreme and unique character).

[Figure 8]

4. Discussion

Functional anatomy and morphology of trabecular bone. While it would be an oversimplification to infer the dynamic complexity of a living organism from a single point in time (*e.g.* the moment of death/preservation), often bones are "all we have" (Kivell, 2016). Although the limited calcaneus samples used in this study – for illustration of the algorithm – cannot be viewed as a robust dataset, an intriguing picture nevertheless emerges. According to the Gordon Museum records, one pathologic calcaneus (club foot) never experienced physiological loading as in walking. The other pathologic calcaneus has no mention of abnormal gait, until chronic inflammation afflicted the donor, and then walking became restricted. Coincidentally, the anisotropy pattern found in the nonpathologic calcanei was absent in the club-foot calcaneus, and was vanishing in the ankylosed calcaneus. This observation is consistent with our previous study on the historical examples of foot binding (Reznikov et al., 2017), where the bound-foot calcanei were lacking a consistent, recognizable anisotropy pattern. According to historical records (Al-Akl, 1932; Blake, 1994), the walking ability in individuals with bound feet was restricted to a various extent, ranging from crippled and slow, to fairly functional. These pieces of evidence allow us to suggest that besides the phylogenetically "wired" bone morphology and architecture, and besides the mere weight-bearing function, it is the recurrent and predictable set of forces exerted by muscles that morph and refine the characteristic anisotropy signature. This hypothesis should be systematically tested in the future studies.

All four presumably physiologically loaded calcanei displayed fairly similar features. The mapped anisotropy vectors formed four recognizable bands, the direction of which agreed with the direction of compressive and tensile forces physiologically exerted on the calcaneus, or the physiologic kinetic pattern. The volume fraction distribution in four physiologically loaded calcanei was somewhat different in terms of absolute values, but they largely followed the same trend: higher values associated with the cortical shell at the periphery, and lower values in the trabecular core which appeared generally featureless. In contrast, the two pathologic samples deviated from the recognizable appearance of the control calcanei in disparate directions: the ankylosed calcaneus showed a barely recognizable anisotropy signature and a generally higher volume fraction throughout the calcaneus. Of note, the patchy variation of the volume fraction in the ankylosed specimen could reflect chronic inflammatory changes. Indeed, coarsening of trabecular texture and loss of homogeneity have been reported, attributable to osteoarthritis in other large joints (Chen et al., 2018; Chu et al., 2019). Conversely, the club-foot calcaneus, that was macroscopically very fragile and wasted, showed lower values on both accounts, whether for anisotropy or volume fraction. According to the 3D maps, congenital disuse of the calcaneus rendered it feeble. It is interesting observation to us that both pathologic calcanei were different in distinct ways, perhaps reflecting a classic observation that "… it is possible to fail in many ways, <…> while to succeed is possible only in one way …"(Aristotle, ca. 350 B.C.E.).

Future perspectives for trabecular anisotropy mapping. The inner architecture of bone responds to loading by load-adaptive remodeling, driven by bone cell ensembles which resorb and deposit micrometer-scale packets of mineralized extracellular matrix (Christen et al., 2014; Currey, 2002; Parfitt, 2006). Such minuscule refinements accumulate over time, leaving a record of an organism's life history. The functional adaptation of bone is thus a multidimensional phenomenon: at the least, there are three dimensions for morphology (X, Y and Z), one for time, one for volume fraction, and two for anisotropy.

Indeed, by comparing the volume fraction and anisotropy maps of the same specimens, one can find all possible combinations such as high anisotropy with low volume fraction, low anisotropy with high volume fraction, both high or both low. Therefore, in total, we may consider at least seven independent parameters when reconstructing the mode of locomotion, past lifestyle, or specific physical activities. These are independent "axes" of adaptation: a bone can possess a robust or gracile morphology, combined with a low or high volume fraction, and with a low or high degree of anisotropy. Many independent combinations are obviously possible, and the independent parameters can be metaphorically likened to "dials", a combination of settings in all of which contributes to the net biomechanical properties. Therefore, using a reduced set of parameters (let's say, only the outer morphology in 3D) is operationally facile, but it drives a question into an impasse that is sometimes referred to as equifinality. For example, is the overall 3D robustness of a bone a result of its owner being old, or of having a large body size, or is it a product of a certain stereotypic activity? Although a tool that allows the generation of hundreds of thousands of additional measurements seemingly does not make the analysis of functional adaptations straightforward, it may prove helpful in unraveling additional dimensions of the convergent process of functional adaptation. Firstly, multidimensional problems can be sorted by dimensionality collapse. For example, perhaps it is possible to register two homologous vector fields and to identify the principle components. Or perhaps it is possible to construct a super-average vector field from multiple homologous specimens – then other individual specimens can be compared to the averaged "template", and the magnitude and localizations of deviations from the template could be used for analysis. Secondly, comparison can be conducted in a reciprocal space, where not the actual space data is presented, but its spectral signature is presented – in a way similar to how Fourier transform of an image can be used to estimate the repetition of periodic features, their size and orientation. A prototype of presenting anisotropy in a reciprocal space would be the anisotropy rose diagram (Ketcham & Ryan, 2004). Thirdly, the arrival of neural networks and deep learning into the domain of image processing is certainly not limited to the segmentation of artifact-plagued scans. The forte of deep learning lies in its ability to parse meaningful abstract features from a multidimensional context. It is therefore exciting to witness the explosion of analytical opportunities that become available for solving the many riddles of bones.

5. Limitations

From the technical method aspect applied here, this study illustrates the great potential of coupling quantitative image analysis and deep learning with priceless museum skeletal collections for valuable research on structure-function relationships in bone using unique and rare exhibits that cannot be otherwise obtained in the modern world. Beyond this unique advantage, contemporary image processing methods that rely on deep learning can be of great utility to enhance image quality and to remove artifacts from X-ray beam hardening-causing added materials applied to a specimen. On the other hand, digital methods obviously cannot reconstruct a specimen's interior damage or missing components that arose from its past handling (Reznikov, Buss, Provencher, McKee, & Piche, 2020). A more specific limitation of this study is that (unfortunately) the biological profile of the donors (*e.g.* age, sex) is unknown to us, which were it available would provide additional insight into our analyses and interpretations. The only limited discriminator we could apply was "presumably nonpathologic" versus "obviously pathologic".

As well, the number of the rare specimens used in this technical note was very small, being only one for each pathologic condition, and four for the nonpathologic calcanei. The extreme character of pathologic changes in the one-of-a-kind historical specimens prevents us from proclaiming overarching conclusions related to biomechanics, but it is nevertheless suitable for testing the sensitivity of the mapping algorithm. It remains possible that even finer details of the anisotropy pattern could emerge in a study comparing 3D anisotropy maps of bones obtained from the donors of known biological profile and lifestyle, and this is something we are currently undertaking.

6. Conclusions

There are several canonical morphometric descriptors of trabecular bone that are accurate as long as trabecular bone is assumed to be homogeneous, uniform and sampled in geometrically regular chunks. To account for a more realistic picture of bones having anatomically distinct 3D shape, accommodating local variation of trabecular texture, and containing natural discontinuities, a high-resolution 3D mapping method for such morphometric properties can be advantageous. The vector field-based 3D mapping algorithm presented here highlights the 3D anisotropic signature of the nonpathologic calcaneus, that is *i*) consistent with the kinetic pattern of compressive and tensile forces acting upon the calcaneus, and *ii*) is covert in a 3D tomographic image of the calcaneus. Moreover, the two extreme pathologic cases of the calcaneus (museum artifacts of club foot and ankylosis used for illustrative purposes) showed substantial deviation from the control morphometric pattern, and were also different from each other. Application of the 3D mapping algorithm to a *bona fide* biomechanical study or a controlled age series of human or animal bones might reveal new trajectories for the functional adaptation of bone to loading.

Acknowledgements

We gratefully thank William Edwards (Gordon Museum of Pathology, King's College London, UK) for giving access to the pathology collection preparations (club foot and ankylosis), Farah Ahmed and Amin Garbout (Natural History Museum, London, UK) for µCT scanning of the Gordon Museum preparations, and Mathieu Gendron (Object Research Systems Inc, Montreal, Quebec, Canada) for coding the 3D mapping application in the Dragonfly™ software. This work was supported by internal funds from McGill University. Marc McKee is the Canada Research Chair in Biomineralization. Natalie Reznikov and Marc McKee are members of the Réseau de recherche en Santé Buccodentaire et Osseuse and the Centre de Recherche en Biologie Structurale funded in part by the Fonds de Recherche du Québec - Santé.

Data are available by request, addressed to the corresponding author.

Author contributions

Natalie Reznikov: Conceptualization, Data curation, Formal analysis, Funding acquisition, Investigation, Methodology, Project administration, Resources, Software, Validation, Visualization, Supervision, Writing - original draft, Writing - review & editing.
Huilin Liang: Data curation, Formal analysis, Investigation, Visualization, Writing - review & editing.
Marc McKee: Project administration, Resources, Supervision, Writing - review & editing.
Nicolas Piché: Conceptualization, Data curation, Formal analysis, Methodology, Resources, Software, Validation, Visualization, Writing - review & editing.

References

Acquaah, F., Robson Brown, K. A., Ahmed, F., Jeffery, N., & Abel, R. L. (2015). Early trabecular development in human vertebrae: overproduction, constructive regression, and refinement. *Frontiers in Endocrinology, 6*, 10.3389/fendo.2015.00067. doi:10.3389/fendo.2015.00067

Al-Akl, F. M. (1932). Bound feet in China. *Am J Surg, 13*(3), 545-550.

Aristotle. (ca. 350 B.C.E.). Book II. In *Nicomachean Ethics*.

Barak, M. M., Lieberman, D. E., & Hublin, J.-J. (2011). A Wolff in sheep's clothing: trabecular bone adaptation in response to changes in joint loading orientation. *Bone, 49*, 1141-1151.

Barak, M. M., Lieberman, D. E., Raichlen, D., Pontzer, H., Warrener, A., & Hublin, J.-J. (2013). Trabecular evidence for a human-like gait in australopithecus africanus. *PLoS ONE, 8*(11), e77687. doi:10.1371/journal.pone.0077687

Barak, M. M., Sherratt, E., & Lieberman, D. E. (2017). Using principal trabecular orientation to differentiate joint loading orientation in the 3rd metacarpal heads of humans and chimpanzees. *J Hum Evol, 113*, 173-182. doi:10.1016/j.jhevol.2017.08.018

Blake, C. F. (1994). Foot-binding in neo-Confucian China and the appropriation of female labor. *Signs, 19*(3), 676-712.

Bouxsein, M. L., Boyd, S. K., Christiansen, B. A., Guldberg, R. E., Jepsen, K. J., & Mueller, R. (2010). Guidelines for assessment of bone microstructure in rodents using micro-computed tomography. *J Bone Miner Res, 25*(7), 1468-1486. doi:10.1002/jbmr.141

Buie, H. R., Campbell, G. M., Klinck, R. J., MacNeil, J. A., & Boyd, S. K. (2007). Automatic segmentation of cortical and trabecular compartments based on a dual threshold technique for in vivo micro-CT bone analysis. *Bone, 41*(4), 505-515. doi:10.1016/j.bone.2007.07.007

Chen, Y., Hu, Y., Yu, Y. E., Zhang, X., Watts, T., Zhou, B., . . . Guo, X. E. (2018). Subchondral trabecular rod loss and plate thickening in the development of osteoarthritis. *J Bone Miner Res, 33*(2), 316-327.

Christen, P., Ito, K., Ellouz, R., Boutroy, S., Sornay-Rendu, E., Chapurlat, R. D., & Van Rietbergen, B. (2014). Bone remodeling in humans is load-driven but not lazy. *Nat Commun, 5:4855* doi:doi: 10.1038/ncomms5855

Chu, L., Lui, X., He, Z., Han, X., Yan, M., Qu, X., . . . Yu, Z. (2019). Articular cartilage degradation and aberrant subchondral bone remodeling in patients with osteoarthritis and osteoporosis. *J Bone Miner Res, in press*.

Currey, J. D. (2002). *Bones: Structure and Mechanics* (2nd ed. ed.). Oxford: Princeton University Press.

Doershuk, L. J., Saers, J. P. P., Shaw, C. N., Jashashvili, T., Carlson, K. J., Stock, J. T., & Ryan, T. M. (2019). Complex variation of trabecular bone structure in the proximalhumerus and femur of five modern human populations. *Am J Phys Anthrop, 168*, 104-118. doi:10.1002/ajpa.23725

Farid, A., & Faber, F. W. M. (2019). Bilateral triple talocalcaneal, calcaneonavicular, and talonavicular tarsal coalition: a case report. *J Foot Anckle Surg, 58*(2), 374-376.

Gefen, A., & Seliktar, R. (2004). Comparison of the trabecular architecture and the isostatic stress flow in the human calcaneus. *Med Eng Phy, 26*, 119-129. doi:10.1016/j.medengphy.2003.10.003

Gibson, L. J., & Ashby, M. F. (2001). *Cellular solids. Structure and properties*. Cambridge, UK: Cambridge University Press.

Goldstein, S. A., Goulet, R., & McCubbrey, D. (1993). Measurement and significance of three-dimensional architecture to the mechanical integrity of trabecular bone *Calcif Tissue Int, 53*(1), S127-S133.

Gross, T., Kivell, T. L., Skinner, M. M., Nguyen, N. H., & Pahr, D. H. (2014). A CT-image-based framework for the holistic analysis of cortical and trabecular bone morphology. *Paleontol Electron, 17*. doi:10.26879/438

Harrigan, T. P., Jasty, M., Mann, R. W., & Harris, W. H. (1988). Limitations of the continuum assumption in cancellous bone. *J Biomech, 21*(4), 269-275.

Herd, F., Macnicol, M., & Abboud, R. J. (2004). The need for biomechanical evaluation in the assessment of clubfoot. *The Foot, 14*(2), 72-76.

Ketcham, R. A., & Ryan, T. M. (2004). Quantification and visualization of anisotropy in trabecular bone. *J Microscopy, 213*(2), 158-171. doi:10.1111/j.1365-2818.2004.01277.x

Kivell, T. L. (2016). A review of trabecular bone functional adaptation:what have we learned from trabecular analyses inextant hominoids and what can we apply to fossils? *J Anat, 228*, 569-594. doi:10.1111/joa.12446

Kuo, S., Desilva, J. M., Devlin, M. J., Mcdonald, G., & Morgan, E. F. (2013). The effect of the achilles tendon on trabecular structure in the primate calcaneus. *Anat Rec, 296*, 1509-1517. doi:10.1002/ar.22739

Maga, M., Kappelman, J., Ryan, T. M., & Ketcham, R. A. (2006). Preliminary observations on the calcaneal trabecular microarchitecture of extant large-bodied hominoids. *Am J Phys Anthrop, 129*, 410-417. doi:10.1002/ajpa.20276

Maquer, G., Musy, S. N., Wandel, J., Gross, T., & Zysset, P. K. (2015). Bone volume fraction and fabric anisotropy are better determinants of trabecular bone stiffness than other morphological variables. *J Bone Miner Res, 30*(6), 1000-1008. doi:10.1002/jbmr.2437

Miedzybrodzka, Z. (2003). Congenital talipes equinovarus (clubfoot): a disorder of the foot but not the hand. *J Anat, 202*(1), 37-42.

Odgaard, A. (1997). Three-dimensional methods for quantification of cancellous bone architecture. *Bone, 20*(4), 315-328. doi:10.1016/s8756-3282(97)00007-0

Odgaard, A. (2001). Quantification of cancellous bone architecture. In C. p. LCC (Ed.), *Bone Mechanics*.

Pahr, D. H., & Zysset, P. K. (2009). From high-resolution CT data to finite element models: development of an integrated modular framework. *Comp Methods Biomech Biomed Engrg, 12*(1), 45-57. doi:10.1080/10255840802144105

Parfitt, A. M. (2006). Misconceptions V—Activation of osteoclasts is the first step in the bone remodeling cycle. *Bone, 39*, 1170-1172.

Paton, R. W., Fox, A. E., Foster, A., & Fehily, M. (2010). Incidence and aetiology of talipes equino-varus with recent population changes. *Acta Orthop Belg, 76*, 86-89.

Pontzer, H., Lieberman, D. E., Momin, E., Devlin, M. J., Polk, J. D., Hallgrimsson, B., & Cooper, D. M. L. (2006). Trabecular bone in the bird knee responds with high sensitivity to changes in load orientation. *J Exp Biol, 209*(1), 57-65.

Raichlen, D., Gordon, A. D., Foster, A. D., Webber, J. T., Sukhdeo, S. M., Scott, R. S., . . . Ryan, T. M. (2015). An ontogenetic framework linking locomotion and trabecular bonearchitecture with applications for reconstructing hominin life history. *J Hum Evol, 81*, 1-12. doi:10.1016/j.jhevol.2015.01.003

Reznikov, N., Buss, D. J., Provencher, B., McKee, M. D., & Piche, N. (2020). Deep learning for 3D imaging and image analysis in biomineralization research. *J Struct Biol, 212*, 107598. doi:10.1016/j.jsb.2020.107598

Reznikov, N., Phillips, C., Cooke, M., Garbout, A., Ahmed, F., & Stevens, M. M. (2017). Functional adaptation of the calcaneus in historical foot binding. *J Bone Miner Res, 32*(9), 1915-1925. doi:10.1002/jbmr.3185

Rogers, M. (1988). Dynamic biomechanics of the normal foot and ankle during walking and running. *Physical Therapy, 68*, 1822-1830.

Ryan, T. M., & Krovitz, G. E. (2006). Trabecular bone ontogeny in the human proximal femur. *J Hum Evol, 51*, 591-602. doi:10.1016/j.jhevol.2006.06.004

Saers, J. P. P., Cazorla-Bak, Y., Shaw, C., Stock, J. T., & Ryan, T. M. (2016). Trabecular bone structural variation throughout the human lower limb. *J Hum Evol, 97*, 97-108. doi:10.1016/j.jhevol.2016.05.012

Saers, J. P. P., Ryan, T. M., & Stock, J. T. (2020). Baby steps towards linking calcaneal trabecular boneontogeny and the development of bipedal human gait. *J Anat, 236*, 474-492. doi:10.1111/joa.13120

Sinclair, K. D., Farnsworth, R. W., Pham, T. X., NKnight, A. N., Bloebaum, R. D., & Skedros, J. G. (2013). The artiodactyl calcaneus as a potential 'control bone' cautions against simple interpretations of trabecular bone adaptation in the anthropoid femoral neck. *J Hum Evol, 64*, 366-379. doi:10.1016/j.jhevol.2013.01.003

Skedros, J. G., Hunt, K. J., & Bloebaum, R. D. (2004). Relationships of loading history and structural and material characteristics of bone: development of the mule deer calcaneus. *J Morphol, 259*(3), 281-307.

Sukhdeo, S. M., Parsons, J., Niu, X. M., & Ryan, T. M. (2020). Trabecular bone structure in the distal femur of humans, apes, and baboons. *Anat Rec, 303*, 129-149. doi:10.1002/ar.24050

Wolff, J. (1892). *Das Gesetz der Transformation der Knochen*. Berlin: Verlag von August Hirschwald.

Figure legends

Figure 1. Human foot specimens. A – Club foot, or talipes varus (Gordon Museum of Pathology, King's College London, UK), with an original description from the museum catalogue. Note the calcaneus is oriented nearly upwards. B – Representative 2D image from the club foot scan. Bony trabeculae are very delicate, and the metal elements used to connect the foot bones (black arrowheads in A) generate pronounced X-ray beam-hardening artifacts during µCT (white arrowheads). C – Calcaneonavicular ankylosis (Gordon Museum of Pathology, King's College London, UK), with an original description from the museum catalogue. All the ankylosed bones are fused into one single aggregate, so no wire mounting was required. However, the µCT image was of poor contrast. D – Modern nonpathologic human foot (Imperial College London, anatomy teaching collection). This specimen was mounted with metal fixtures (black arrowheads), and the beam-hardening artifacts from this are evident in panel E (white arrowheads).

Figure 2. Surface rendering of 3 specimens. Two historical specimens are rendered in full (A, C), in addition to the focused scans of the calcanei (B, D, E). In the full-size scans, individual bones are color-coded for ease of identification. The position of the bounding boxes used for all the analyses is shown in panels B, D, and E, and they are centered in the sagittal plane (or would-be sagittal in B).

Figure 3. Comparison of the 3D anisotropy maps constructed over the same 3D image of trabecular bone using different sampling volumes. The maps are visualized by the vector magnitude. The sampling volume increases from 0.1 mm to 2.3 mm (from A to G). Anisotropic bands become apparent when the sampling radius exceeds 0.5 mm, and they become progressively smoother as the sampling radius increases. The speed of computation decreases as the sampling radius increases. Conversely, reducing the bounding box volume reduces the computation time.

Figure 4. Comparison of the 3D anisotropy maps constructed over the same 3D image of trabecular bone using different sampling volumes. The maps are visualized by the vector orientation with respect to the principal axes. The sampling volume increases from 0.1 mm to 2.3 mm (from A to G). Anisotropic bands become apparent when the sampling radius exceeds 0.5 mm, and become progressively smoother as the sampling radius increases.

Figure 5. Anatomical context for 3D maps of calcaneus. A – Surface-rendered nonpathologic calcaneus is shown in its anatomical position (posterior-lateral aspect). The arrows indicate the pulling direction of the Achilles tendon and the plantar fascia. The area enclosed in the cubic box is enlarged in panel B. B – Trabecular texture of the calcaneal tuberosity. Note the absence of visible vestiges of the growth plate. C and D – Anisotropy vector fields constructed over the fragment presented in panel B, color-coded by magnitude and direction, respectively. E – The 3D anisotropy vector field is partly clipped to expose its interior and is inscribed in the semi-transparent mesh rendering of the calcaneus. F – Only the high-magnitude (0.7-0.8) anisotropy vectors are highlighted. Note the presence of the stereotypical anisotropy bands. G – In the same volume, only the low magnitude anisotropy (0-0.3) are presented. Note the complementary distribution with respect to F, and the visibility of the growth plate location which is not readily visible in panel B.

Figure 6. Three nonpathologic human calcanei, sagittal view. Each row illustrates the maps produced from one calcaneus. The left column shows the variation of BV/TV in 3D; in all three specimens, the highest local volume fraction can be found in the subtalar area (asterisk in panel A), although inter-individual variation is apparent. The middle column shows local anisotropy plotted by magnitude. Note

that highest local volume fraction, and highest local anisotropy, do not necessarily coincide. Three principal bands can be seen in the sagittal plane: dorsal, plantar and Achilles' bands. The right column shows the same vector fields as the middle column, but the vectors are color-coded by direction. The green left-of-center formation in all three direction maps (panels C,F and I) corresponds to the band of trabeculae oriented perpendicular to the plane of the image, apparently in the direction of the calcaneo-fibular and peroneal ligament attachment.

Figure 7. One nonpathologic and two pathologic calcanei, sagittal view. The nonpathologic calcaneus is different from those presented in Figure 6. Note that in the case of congenital disuse (club foot), both volume fraction and anisotropy are lost. In the case of acquired disuse (ankylosis), the local values of volume fraction are higher and more diverse, while the local anisotropy pattern appears to be vanishing in comparison with the typical pattern, although still recognizable (both in terms of magnitude and direction).

Figure 8. Comparison of mode values of the volume fraction values (A) and anisotropy values (B). A – The modal values (indicated by vertical lines) of the volume fraction vary between 0.05 and 0.175, of which the club foot has the lowest value and the ankylosed calcaneus has the highest value. B – The modal values of anisotropy (also indicated by vertical lines) cluster together for nonpathologic cases between 0.6 and 0.675, whereas the ankylosed calcaneus has a lower modal value of 0.45, and the club foot calcaneus has the lowest modal value of 0.31. Plot lines are color-coded as in panel B.

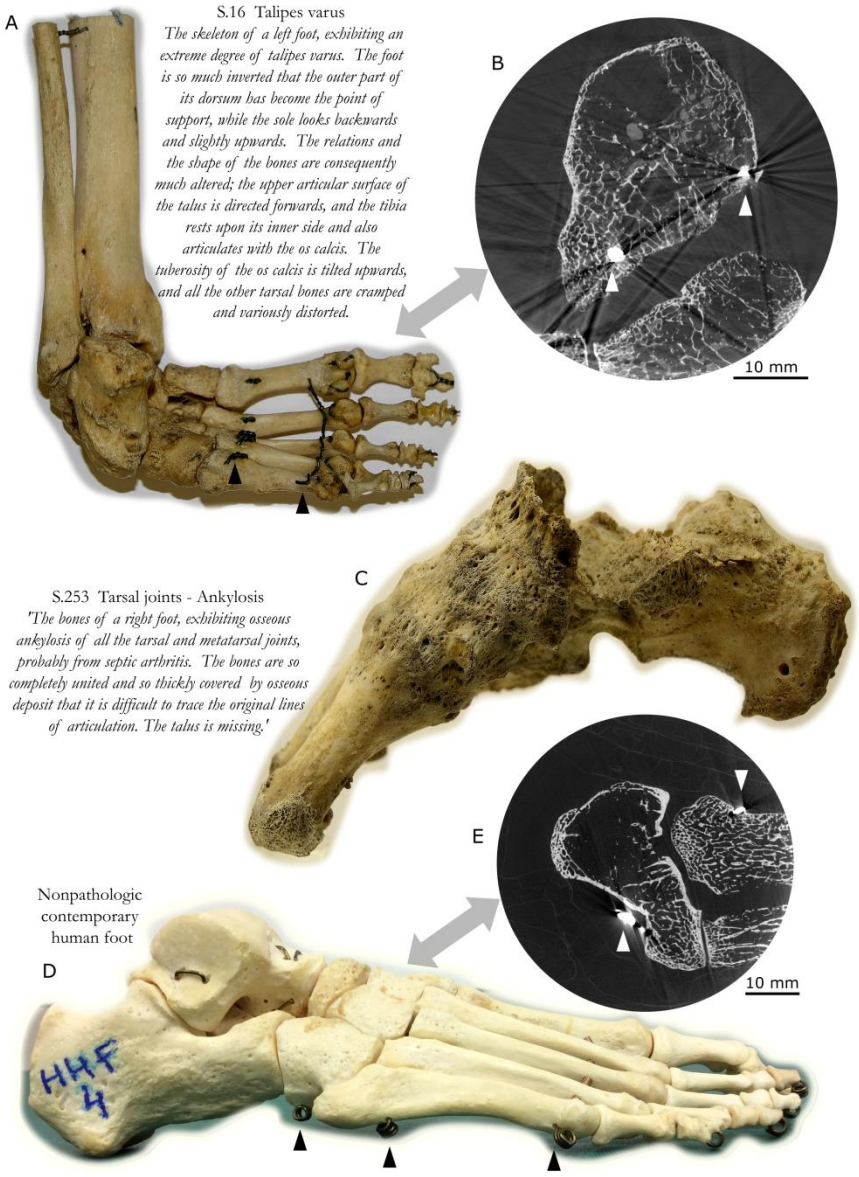

Figure 1. Human foot specimens. A – Club foot, or talipes varus (Gordon Museum of Pathology, King's College London, UK), with an original description from the museum catalogue. Note the calcaneus is oriented nearly upwards. B – Representative 2D image from the club foot scan. Bony trabeculae are very delicate, and the metal elements used to connect the foot bones (black arrowheads in A) generate pronounced X-ray beam-hardening artifacts during μCT (white arrowheads). C – Calcaneonavicular ankylosis (Gordon Museum of Pathology, King's College London, UK), with an original description from the museum catalogue. All the ankylosed bones are fused into one single aggregate, so no wire mounting was required. However, the μCT image was of poor contrast. D – Modern nonpathologic human foot (Imperial College London, anatomy teaching collection). This specimen was mounted with metal fixtures (black arrowheads), and the beam-hardening artifacts from this are evident in panel E (white arrowheads).

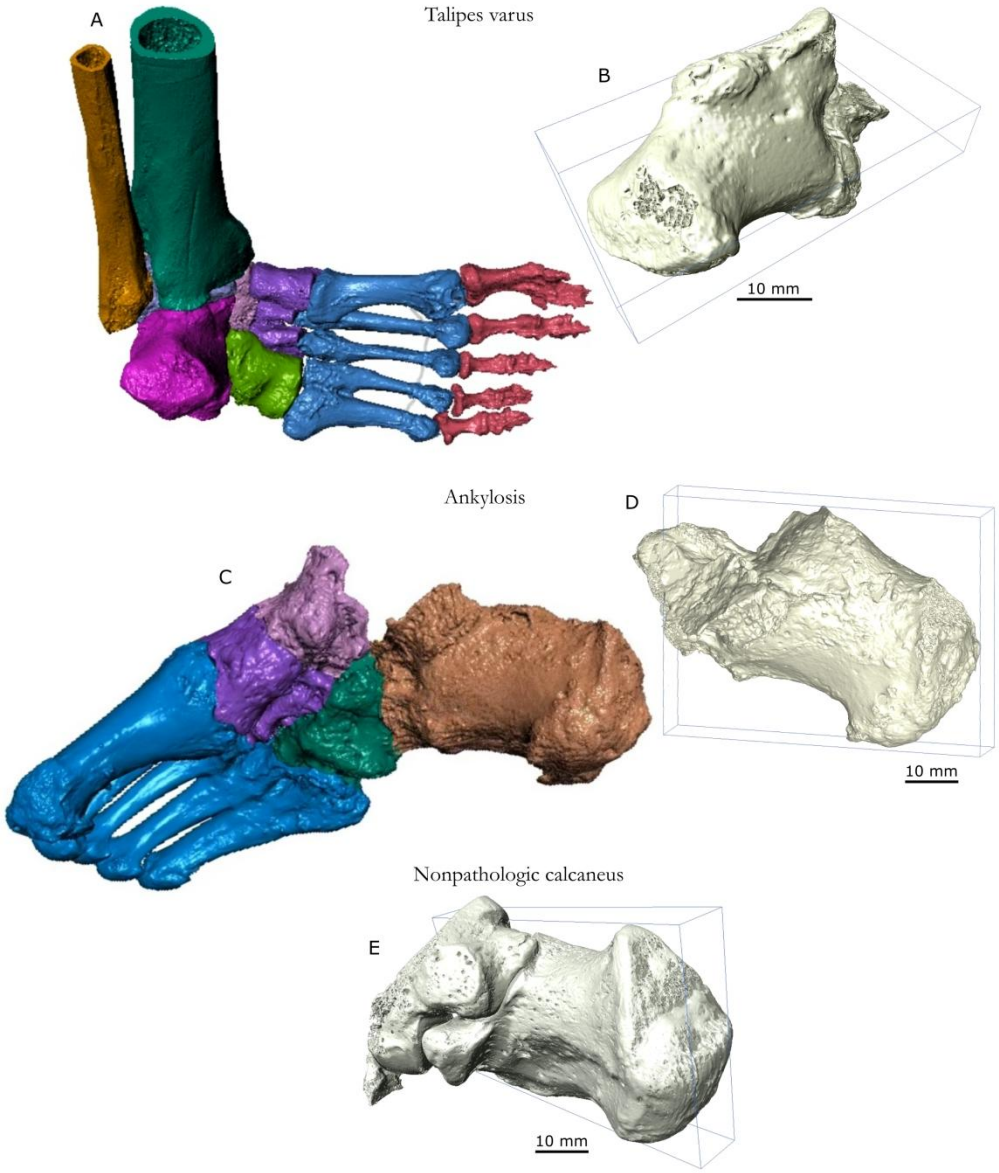

Figure 2. Surface rendering of 3 specimens. Two historical specimens are rendered in full (A, C), in addition to the focused scans of the calcanei (B, D, E). In the full-size scans, individual bones are color-coded for ease of identification. The position of the bounding boxes used for all the analyses is shown in panels B, D, and E, and they are centered in the sagittal plane (or would-be sagittal in B).

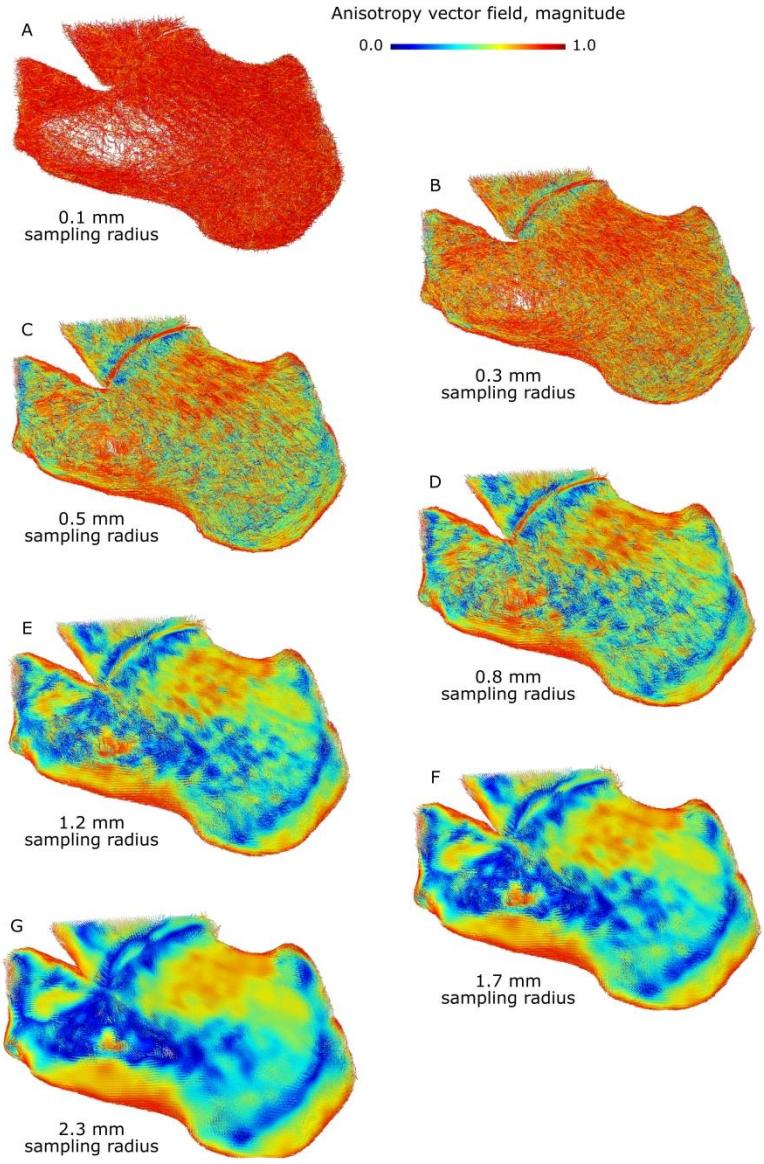

Figure 3. Comparison of the 3D anisotropy maps constructed over the same 3D image of trabecular bone using different sampling volumes. The maps are visualized by the vector magnitude. The sampling volume increases from 0.1 mm to 2.3 mm (from A to G). Anisotropic bands become apparent when the sampling radius exceeds 0.5 mm, and they become progressively smoother as the sampling radius increases. The speed of computation decreases as the sampling radius increases. Conversely, reducing the bounding box volume reduces the computation time.

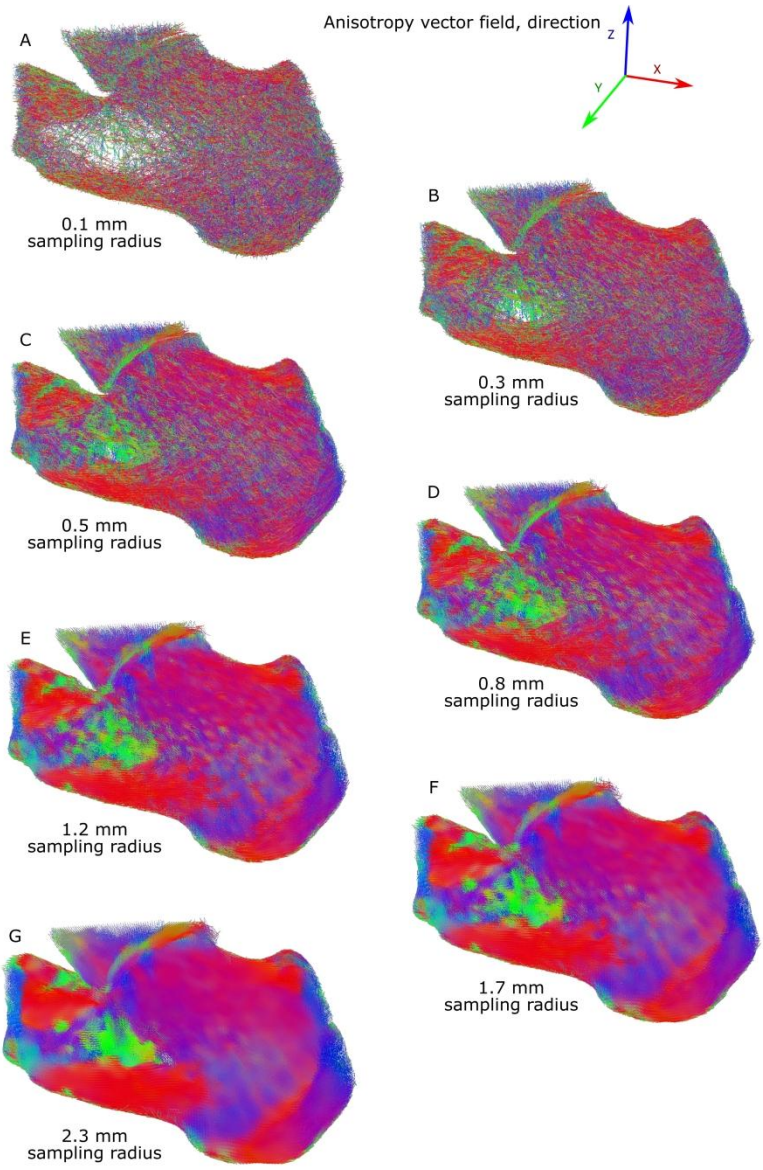

Figure 4. Comparison of the 3D anisotropy maps constructed over the same 3D image of trabecular bone using different sampling volumes. The maps are visualized by the vector orientation with respect to the principal axes. The sampling volume increases from 0.1 mm to 2.3 mm (from A to G). Anisotropic bands become apparent when the sampling radius exceeds 0.5 mm, and become progressively smoother as the sampling radius increases.

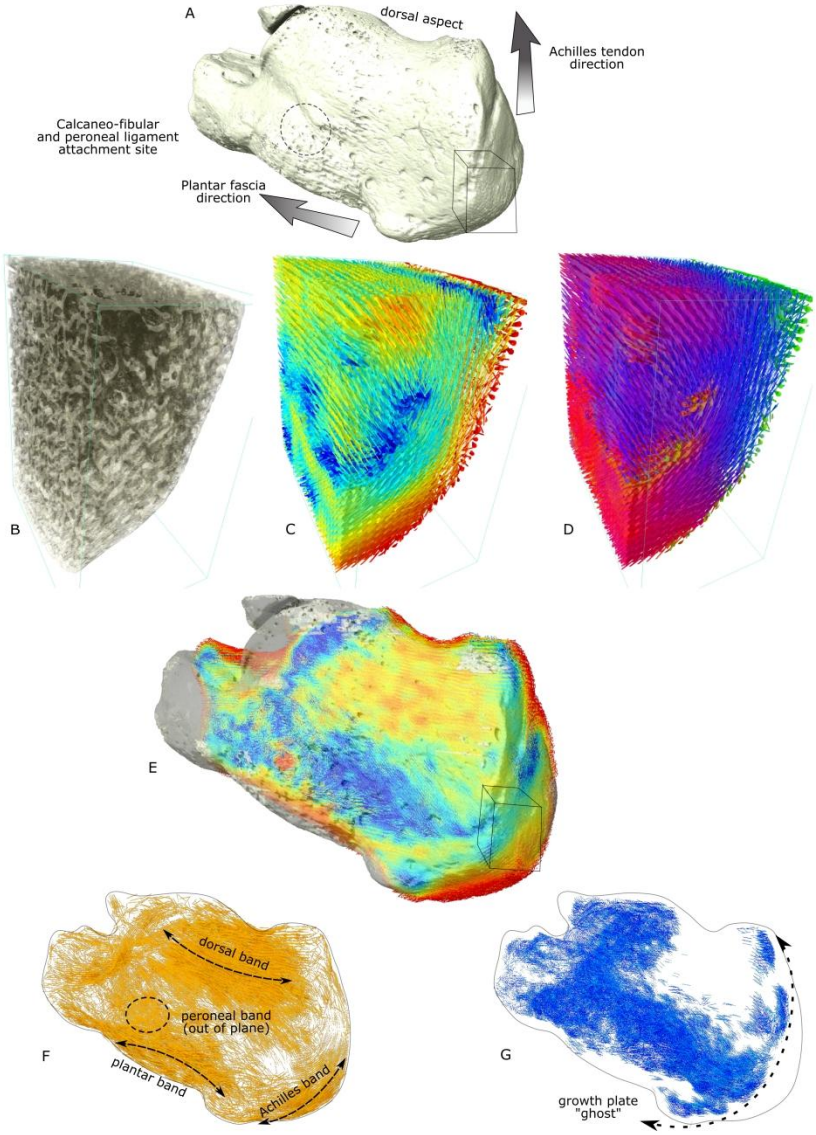

Figure 5. Anatomical context for 3D maps of calcaneus. A – Surface-rendered nonpathologic calcaneus is shown in its anatomical position (posterior-lateral aspect). The arrows indicate the pulling direction of the Achilles tendon and the plantar fascia. The area enclosed in the cubic box is enlarged in panel B. B – Trabecular texture of the calcaneal tuberosity. Note the absence of visible vestiges of the growth plate. C and D – Anisotropy vector fields constructed over the fragment presented in panel B, color-coded by magnitude and direction, respectively. E – The 3D anisotropy vector field is partly clipped to expose its interior and is inscribed in the semi-transparent mesh rendering of the calcaneus. F – Only the high-magnitude (0.7-0.8) anisotropy vectors are highlighted. Note the presence of the stereotypical anisotropy bands. G – In the same volume, only the low magnitude anisotropy (0-0.3) are presented. Note the complementary distribution with respect to F, and the visibility of the growth plate location which is not readily visible in panel B.

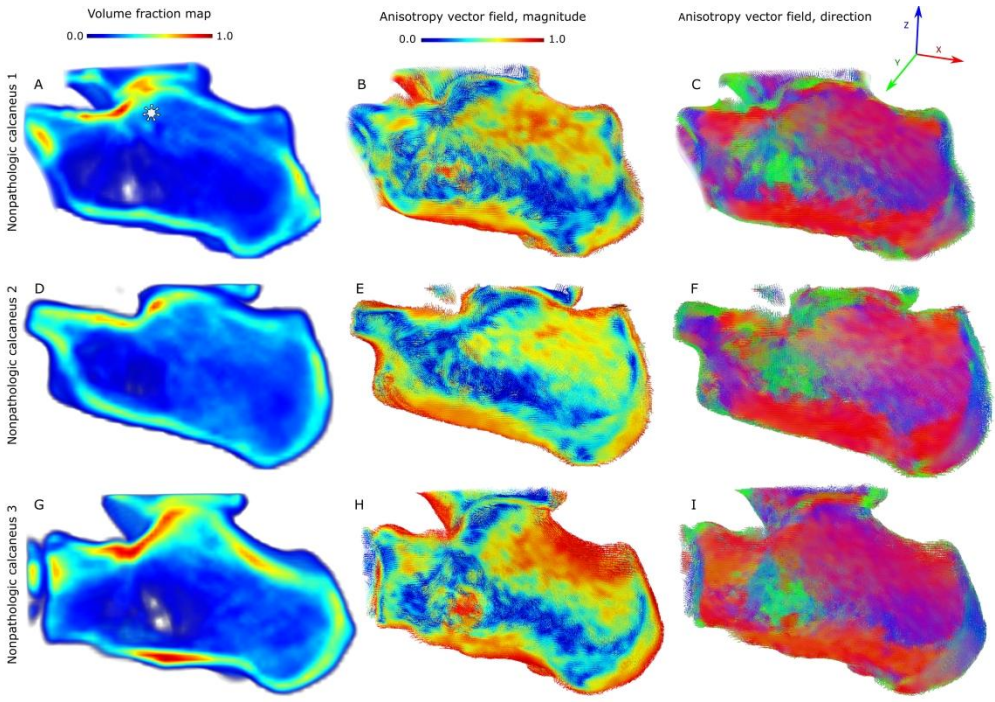

Figure 6. Three nonpathologic human calcanei, sagittal view. Each row illustrates the maps produced from one calcaneus. The left column shows the variation of BV/TV in 3D; in all three specimens, the highest local volume fraction can be found in the subtalar area (asterisk in panel A), although inter-individual variation is apparent. The middle column shows local anisotropy plotted by magnitude. Note that highest local volume fraction, and highest local anisotropy, do not necessarily coincide. Three principal bands can be seen in the sagittal plane: dorsal, plantar and Achilles' bands. The right column shows the same vector fields as the middle column, but the vectors are color-coded by direction. The green left-of-center formation in all three direction maps (panels C,F and I) corresponds to the band of trabeculae oriented perpendicular to the plane of the image, apparently in the direction of the calcaneo-fibular and peroneal ligament attachment.

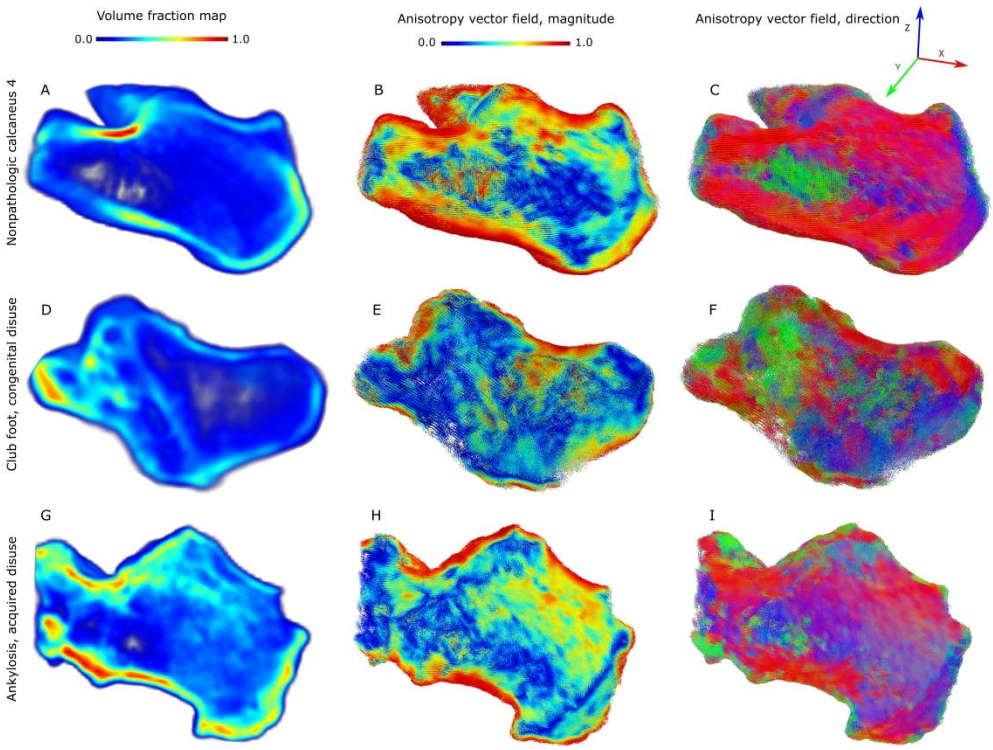

Figure 7. One nonpathologic and two pathologic calcanei, sagittal view. The nonpathologic calcaneus is different from those presented in Figure 6. Note that in the case of congenital disuse (club foot), both volume fraction and anisotropy are lost. In the case of acquired disuse (ankylosis), the local values of volume fraction are higher and more diverse, while the local anisotropy pattern appears to be vanishing in comparison with the typical pattern, although still recognizable (both in terms of magnitude and direction).

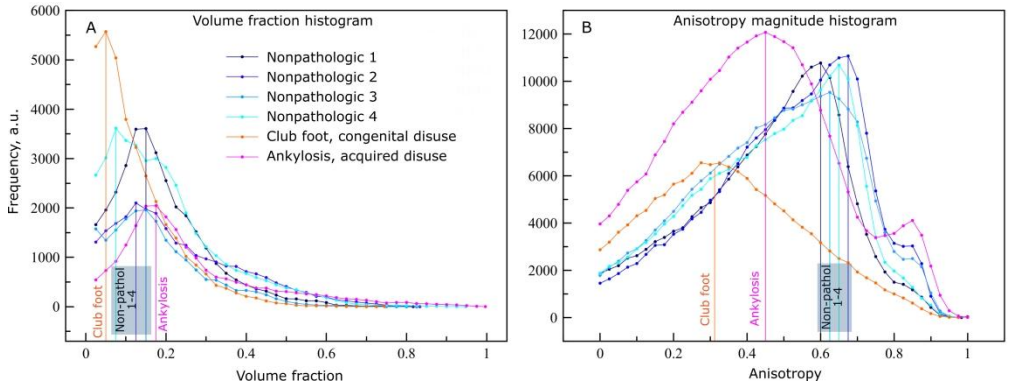

Figure 8. Comparison of mode values of the volume fraction values (A) and anisotropy values (B). A – The modal values (indicated by vertical lines) of the volume fraction vary between 0.05 and 0.175, of which the club foot has the lowest value and the ankylosed calcaneus has the highest value. B – The modal values of anisotropy (also indicated by vertical lines) cluster together for nonpathologic cases between 0.6 and 0.675, whereas the ankylosed calcaneus has a lower modal value of 0.45, and the club foot calcaneus has the lowest modal value of 0.31. Plot lines are color-coded as in panel B.